https://doi.org/10.1016/j.jpowsour.2020.227831

Harvesting waste heat produced in solid oxide fuel cell using near-field thermophotovoltaic cell

Tianjun Liao[a, b], Qijiao He [a], Qidong Xu [a], Yawen Dai [a], Chun Cheng [a], Meng Ni[a*]

[a] *Department of Building and Real Estate, The Hong Kong Polytechnic University, Hung Hom, Kowloon, Hong Kong, China*

[b] *Department of Physics and Energy, Chongqing University of Technology, Chongqing 400054, China*

Abstract: A coupled system consisting of a regenerator, a solid oxide fuel cell (SOFC), and a near-field thermophotovoltaic cell (NFTC) is proposed to recovery the waste heat from the SOFC. Based on the theories of electrochemical and fluctuation electrodynamics, analytical formulas for the power output and the overall energy conversion efficiency of the coupled system are derived. The dependence of the matching area ratio between the subsystems on the key parameters is discussed. The two voltages of the subsystems are optimized to obtain the maximum power output density through numerical simulation. By comparing to the performance of the single SOFC, the optimally working regions of the coupled system are determined. The effects of the SOFC's temperature and the NFTC's vacuum gap on the maximum power output density and the optimum operating conditions of the system are studied. The comparisons between the present coupled system and the far-field performance limit and the other SOFC-based coupled systems are made. The present work can provide a new route to efficiently utilize the waste heat of SOFC to achieve higher energy efficiency.

Key words: Near-field thermophotovoltaic cell; Solid oxide fuel cell; Waste heat recovery; Coupled system.

*Corresponding author (M. Ni)
Email: meng.ni@polyu.edu.hk; Tel: 852-27664152; Fax: 852-27645131

Nomenclature

A area (cm^{-2})
c speed of light (cms^{-1})
d vacuum gap (nm)
e elementary positive charge (C)
F Faraday's constant ($C mol^{-1}$)
Δg molar Gibbs energy ($Jmol^{-1}$)
$\hbar$ reduced Planck constant (Js)
Δh molar enthalpy change ($J mol^{-1}$)
$-\Delta \dot{H}$ enthalpy change (J)
J current density (Acm^{-2})
$J_{e,a}$ exchange current density of anode (Acm^{-2})
$J_{e,c}$ exchange current density of cathode (Acm^{-2})
$J_{L,a}$ limiting current density of anode (Acm^{-2})
$J_{L,c}$ limiting current density of cathode (Acm^{-2})
K Boltzmann constant (JK^{-1})
k wave vector (cm^{-1})
L_{et} electrolyte thickness (cm)
N number of electrons transferred in reaction
n refraction index
P power output (W)
P^* power density of coupled system (Wcm^{-2})
p_i partial pressure (atm)
q_j heat flow (W)
r Fresnel's coefficients
R universal gas constant ($J mol^{-1}K^{-1}$)
s coupling coefficient (cm^{-1})
T temperature (K)
U heat transfer coefficient ($Wcm^{-2}K^{-4}$)
V voltage (V)
W_{ae} activation energy for ion transport ($J mol^{-1}$)
E photon energy (J)
E_g PV cell bandgap (J)
Z objective function (Wcm^{-2})

Greek symbols

α absorption coefficient (cm^{-1})
β parallel wave vector (cm^{-1})
λ_{th} thermal wavelength (cm)
θ angle (rad)
σ reference ionic conductivity ($S cm^{-1}$)
η efficiency
ε dielectric function (Fcm^{-1})
ω angular frequency ($rads^{-1}$)
ω_g bandgap angular frequency ($rads^{-1}$)
ϕ Bose distribution

Subscript

A ambient
F fuel cell
i H_2, O_2, H_2O
j in, out, leak
N near-field
act activation overpotential
con concentration overpotential
in input
lb low bound
max maximum
ohm ohmic overpotential
P maximum power density point
ub up bound
R radiator
Rev reversible voltage
su start-up
s polarized wave
p polarized wave
V vacuum

Abbreviations

PV photovoltaic
NTPC near-field thermophotovoltaic cell
FFNC far-field thermophotovoltaic cell
SOFC solid oxide fuel cell
Evan evanescent
Prop propagating
FDT fluctuation dissipation theorem
NFRHT near-field radiative heat transfer

1. Introduction

Solid oxide fuel cell (SOFC) is a solid-state power device that converts chemical energy of a fuel into electricity [1]. The SOFCs have attracted tremendous attention due to their high efficiency, low noise, safety, low pollution etc. [2-5]. As SOFCs work at a high temperature such as 800 ^{o}C, the waste heat from the SOFC stack is of high quality and can be recovered by integrating SOFC stacks with other thermal-to-power energy conversion devices to increase the overall energy efficiency of the coupled system. Zhao *et al.* [6] proposed and modeled an SOFC-Carnot heat engine coupled system. The overall thermodynamic performances of the coupled system were optimized, and the optimal operating regions of some key parameters of the system were given. Chen *et al.* [7] studied and evaluated the SOFC-single stage thermoelectric generator (STEG) coupled system. The results showed that the coupled system could efficiently harness the waste heat. Making a trade-off between the power output density and efficiency, the parametric optimal operating regions were given. Zhang *et al.* [8] proposed a method to harness the waste heat in the SOFC based on the two stage-thermoelectric generators (TTEG). The maximum power output density and energy conversion efficiency of the coupled system were determined. The results showed that the TTEG-based coupled system is superior to the STEG-based coupled system only when the SOFC operates at high temperature. Wang *et al.* [9] applied thermionic generator (TIC) to recycle the waste heat in the SOFC. The high work function of the anode limits the power output density of the TIC. The temperature of the anode is set to 600 K due to the black-body radiation and the emission of electrons within the TIC. The above-mentioned factors lead that the maximum power output density of the TIC-based coupled system is smaller than that of the TEG-based coupled systems. In addition, the SOFC can be integrated with gas turbine [10], Braysson [11], and Brayton [12] heat engines and Rankine cycle [13] to recovery its waste heat. Although the performances of above four types systems are superior to the

TEG- and TIC-based coupled systems, these large-scale systems with rotating parts require complex designs, which hinder the development. It is necessary to develop small coupled systems that present high performances and are easy to design. In a recent work, the far-field thermophotovoltaic cell (FFNC) was integrated with SOFC [14]. The maximum power output density was calculated. The optimal operating regions of the coupled system were determined, compared with the performance of the single SOFC. The selection criteria of some key parameters were given. The proposed model can efficiently exploit the waste heat produced in SOFC.

Especially, as the vacuum gap is far less than the characteristic wavelength of thermal radiation given by Wien's displacement law, the near-field thermophtovoltaic cell (NFTC) can efficiently convert high-grade thermal energy into electricity [15]. Based on the NFTC, the conceptual models of TIC-NFTC coupled system have been proposed to improve the thermoelectric conversion efficiency [16-18]. Therefore, it is expected that NFTC can be very promising for utilizing the waste heat of SOFC for additional power generation. However, no research work has been reported on the SOFC-NFTC coupled system yet. In order to fill this research gap, a new SOFC-NFTC coupled system is proposed and theoretically evaluated in this work. Theoretical models are developed to simulate the performances of the NFTC and SOFC. The power output and efficiency of the coupled system are analytically derived. The optimal performance characteristics of the coupled system are discussed in detail. The results are generalized for SOFCs at different operating temperatures and compared with those of other SOFC-based coupled systems.

2. Model description

The SOFC-NFTC coupled system composed of an SOFC, a regenerator, a photon radiator, and a PV cell, as shown in Fig. 1(a). The role of the regenerator in the coupled system is to preheat the incoming air and fuel by using the high-temperature exhaust gas of the SOFC and to ensure that the SOFC works at temperature T_F [6, 18]. The radiator at temperature T_R and PV cell at temperature T_N are, respectively, made of hexagonal Boron Nitride (h-BN) and III-V group semiconductor material InAs (band-gap 0.36 eV) [14]. These two basic elements in the NFTC separated by a vacuum gap d can exchange radiative heat flow q_N. The corresponding heat exchange area is A_N. The SOFC and the radiator are contacted with each other through high thermal conductivity material. The intrinsic mechanism of the coupled system is that the SOFC generates power output P_F and acts as the heat source of the NFTC to generate additional power output P_N. The SOFC releases heat-leak rate q_L and heat flow q_{in} into the ambient and the NTFC, respectively. The infrared photons emitted from the radiator, through the vacuum gap due to photon tunneling effect, are absorbed by the PV cell to generate electron-hole pairs inside the semiconductor, which are extracted to an external circuit to electricity. Simultaneously, the back surface of the PV cell releases the heat flow q_{out} to the ambient. For the convenience of discussion, we assume that the radiator directly contacts with the SOFC and works at a fixed temperature $T_R = T_F$.

The working principle of NFTC is presented in Fig. 1(b), where n_R and n_V denote the refraction indexes. The PV cell is composed of p-type and n-type semiconductors. E_C and E_V are the energy levels at the bottom of the conduction band and top of the valence band, whose difference $(E_C - E_V)$ corresponds the band-gap E_g. E_{fe} and E_{fh} are the quasi-Fermi levels of electrons and holes, whose difference $(E_{fe} - E_{fh})$ corresponds to the voltage output V_N multiplied by an elementary positive charge e. The photo-generated electron-hole pairs can be separated by selective contact electrodes. The electrons flow through the external load to produce useful electricity. The material properties of the radiator and PV cell are described by the frequencies dependent complex dielectric functions $\varepsilon_R(\omega)$ and $\varepsilon_N(\omega)$. The thermal radiation generated by the random thermal motion of particles within an object can be described by the fluctuation dissipation theorem (FDT). By combining of the

Maxwell's equations and the FDT, the fluctuational electrodynamics theory was established to compute the near-field radiative heat transfer (NFRHT). As the incident angle θ_{i} and the reflex angle θ_{r} meet the relation $\theta_{\mathrm{i}}=\theta_{\mathrm{r}}\geq\arcsin\left(n_{\mathrm{R}}/n_{\mathrm{V}}\right)$, the evanescent (Evan) waves contributing to the NFRHT are significantly enhanced under the condition that the vacuum gap d is smaller than the thermal wavelength λ_{th}. Meanwhile, the propagating (Prop) waves contributing to the NFRHT should be taken into consideration as $\theta_{\mathrm{i}}=\theta_{\mathrm{r}}<\arcsin\left(n_{\mathrm{R}}/n_{\mathrm{V}}\right)$. Importantly, the fluctuational electrodynamics theory for calculating for the NFRHT between two semi-infinite plates at different temperatures was experimentally demonstrated [19-21]. Recently, the physical model of the NFTC was theoretically and experimentally studied [22]. Therefore, the similar model can be used to discuss the problem of the optimal coupling between the SOFC and the NFTC.

2.1. The power output and efficiency of an SOFC

The irreversible thermodynamic model of an SOFC has demonstrated that the efficiency η_{F} and the power output P_{F} depend on the number of electrons transferred in reaction $N=2$, the Faraday's constant $F=9.65\times10^{4}\,\mathrm{C\,mol^{-1}}$, the universal gas constant $R=8.314\,\mathrm{J\,mol^{-1}K^{-1}}$, the current density J_{F}, the operating voltage V_{F}, and the surface area of the contact electrode A_{F} etc. The formulas for η_{F} and P_{F} are, respectively, presented as [23-28]

$$\eta_{\mathrm{F}}=\frac{P_{\mathrm{F}}}{-\Delta\dot{H}} \tag{1}$$

and

$$P_{\mathrm{F}}=V_{\mathrm{F}}J_{\mathrm{F}}A_{\mathrm{F}}=\left(V_{\mathrm{Rev}}-V_{\mathrm{act}}-V_{\mathrm{con}}-V_{\mathrm{ohm}}\right)J_{\mathrm{F}}A_{\mathrm{F}}, \tag{2}$$

where $-\Delta\dot{H}=-\Delta hJ_{\mathrm{F}}A_{\mathrm{F}}/(NF)$ represents the total enthalpy change for electrochemical reaction. Δh stands for the molar enthalpy change for electrochemical reaction. The reversible voltage V_{Rev} and irreversible voltage losses including the ohmic overpotential V_{ohm}, concentration overpotential V_{con}, and activation overpotential V_{act}. These overpotential terms can be, respectively, expressed as [23-28]

$$V_{\mathrm{Rev}} = \frac{RT_{\mathrm{F}}}{NF}\ln\left(\frac{p_{\mathrm{H_2}}\sqrt{p_{\mathrm{O_2}}}}{p_{\mathrm{H_2O}}}\right) - \frac{\Delta g\left(T_{\mathrm{F}}\right)}{NF}, \tag{3}$$

$$V_{\mathrm{ohm}} = \frac{J_{\mathrm{F}}L_{\mathrm{et}}T_{\mathrm{F}}}{\sigma}\exp\left(\frac{W_{\mathrm{ae}}}{RT_{\mathrm{F}}}\right), \tag{4}$$

$$V_{\mathrm{con}} = -\frac{RT_{\mathrm{F}}}{NF}\left[\ln\left(1-J_{\mathrm{F}}/J_{\mathrm{L,a}}\right)+\ln\left(1-J_{\mathrm{F}}/J_{\mathrm{L,c}}\right)\right], \tag{5}$$

and

$$V_{\mathrm{act}} = \frac{2RT_{\mathrm{F}}}{F}\left[\sinh^{-1}\left(0.5J_{\mathrm{F}}/J_{\mathrm{e,a}}\right)+\sinh^{-1}\left(0.5J_{\mathrm{F}}/J_{\mathrm{e,c}}\right)\right], \tag{6}$$

where $\Delta g\left(T_{\mathrm{F}}\right)$ means the molar Gibbs energy change under the standard atmospheric pressure. $p_{\mathrm{H_2}}$, $p_{\mathrm{O_2}}$, and $p_{\mathrm{H_2O}}$ are, respectively, the partial pressures of the hydrogen, oxygen, and water. $J_{\mathrm{e,a}}$ and $J_{\mathrm{e,c}}$ are, respectively, the exchange current densities of the anode and cathode. $J_{\mathrm{L,a}}$ and $J_{\mathrm{L,c}}$ represent the limiting current densities of the anode and cathode. L_{et}, W_{ae}, and σ are, respectively, the electrolyte thickness, the activation energy for ion transport and the reference ionic conductivity. The performance parameters of the SOFC are listed in Table 1.

2.2. The power output of a NFTC

The two dielectric functions $\varepsilon_{\mathrm{R}}\left(\omega\right)$ and $\varepsilon_{\mathrm{N}}\left(\omega\right)$ of the radiator and the PV cell can be described as [15]

$$\varepsilon_{\mathrm{R}}\left(\omega\right) = 4.88\left[\frac{\omega^2-(3.032\times10^{14})^2+1.001\times10^{12}\omega i}{\omega^2-(2.575\times10^{14})^2+1.001\times10^{12}\omega i}\right] \tag{7}$$

and

$$\varepsilon_{\mathrm{N}}\left(\omega\right) = \begin{cases} n_{\mathrm{N}}, & \omega<\omega_g \\ \left[n_{\mathrm{N}}+\left(ic\alpha\sqrt{\omega/\omega_g-1}\right)\left(2\omega\right)^{-1}\right]^2, & \omega\geq\omega_g \end{cases}, \tag{8}$$

where n_{N}=3.51 is the refractive index of the PV cell. ω is the angular frequency. α is the absorption coefficient [8]. ω_{g} is the band-gap frequency of the PV cell. c is the speed of light.

According to the fluctuation electrodynamics theory, the Prop and Evan waves in the vacuum gap generate the NFRHT flows q_{Prop} and q_{Evan}, i.e., [19-22, 29]

$$q_{\text{Prop}} = \frac{A_{\text{N}}}{\pi^2}\int_0^{\infty}\frac{d\omega}{2\pi}\left[\phi(\omega,T_{\text{R}})-\phi(\omega-\omega_0,T_{\text{N}})\right]\hbar\omega\times\int_0^{\omega/c}d\beta s_{\text{Prop}} \tag{9}$$

and

$$q_{\text{Evan}} = \frac{A_{\text{N}}}{\pi^2}\int_0^{\infty}\frac{d\omega}{2\pi}\left[\phi(\omega,T_{\text{R}})-\phi(\omega-\omega_0,T_{\text{N}})\right]\hbar\omega\times\int_{\omega/c}^{\infty}d\beta s_{\text{Evan}}, \tag{10}$$

where the sum of q_{Prop} and q_{Evan} is equal to q_{N}, i.e., $q_{\text{Evan}}+q_{\text{Prop}}=q_{\text{N}}$. β is the parallel wave vector component. $\phi(\omega,T)=1/\left\{\exp\left[\hbar\omega/(KT)\right]-1\right\}$ is the Bose distribution. K is the Boltzmann constant. $\omega_0=0$ means that the PV cell can't generate electron-hole pairs when $\omega<\omega_{\text{g}}$; $\omega_0=V_{\text{N}}e/\hbar$ indicates that the PV cell can generate working voltage V_{N}. e is the elementary positive charge. $\hbar$ is the reduced Planck constant. The two coupling coefficients s_{Evan} and s_{Prop} of evanescent waves and propagating waves can be expressed as [15, 19-22, 31]

$$s_{\text{Evan}} = \frac{\text{Im}(r_{\text{R, p}})\,\text{Im}(r_{\text{N,p}})\beta e^{2ik_{z\text{V}}d}}{\left|1-r_{\text{R, p}}r_{\text{N,p}}e^{2ik_{z\text{V}}d}\right|^2}+\frac{\text{Im}(r_{\text{R,s}})\,\text{Im}(r_{\text{N,s}})\beta e^{2ik_{z\text{V}}d}}{\left|1-r_{\text{R,s}}r_{\text{N,s}}e^{2ik_{z\text{V}}d}\right|^2} \tag{11}$$

and

$$s_{\text{Prop}} = \frac{\beta(1-\left|r_{\text{R, p}}\right|^2)(1-\left|r_{\text{N, p}}\right|^2)}{4\left|1-r_{\text{R, p}}r_{\text{N,p}}e^{2ik_{z\text{V}}d}\right|^2}+\frac{\beta(1-\left|r_{\text{R, s}}\right|^2)(1-\left|r_{\text{N, s}}\right|^2)}{4\left|1-r_{\text{R,s}}r_{\text{N,s}}e^{2ik_{z\text{V}}d}\right|^2}\ , \tag{12}$$

where $r_{\text{R,s}}=\frac{k_{z\text{V}}-k_{z\text{R}}}{k_{z\text{V}}+k_{z\text{R}}}$, $r_{\text{P,s}}=\frac{k_{z\text{V}}-k_{z\text{N}}}{k_{z\text{V}}+k_{z\text{N}}}$, $r_{\text{R,p}}=\frac{\varepsilon_{\text{R}}k_{z\text{V}}-k_{z\text{R}}}{\varepsilon_{\text{R}}k_{z\text{V}}+k_{z\text{R}}}$, and $r_{\text{N,p}}=\frac{\varepsilon_{\text{N}}k_{z\text{V}}-k_{z\text{N}}}{\varepsilon_{\text{N}}k_{z\text{V}}+k_{z\text{N}}}$ denotes the vacuum-medium Fresnel's coefficients. The subscripts s and p represent two polarized waves. $k_{z\text{V}}=\sqrt{(\omega/c)^2-\beta^2}$ is the z component of the wave vector in the vacuum. $k_{z\text{R}}=\sqrt{\varepsilon_{\text{R}}(\omega)(\omega/c)^2-\beta^2}$ and $k_{z\text{N}}=\sqrt{\varepsilon_{\text{N}}(\omega)(\omega/c)^2-\beta^2}$ are the z components of the wave vectors inside the radiator and the PV cell.

When the PV cell is in operation, the current density J_{N} is computed as [22, 30, 31]

$$J_{\text{N}} = \frac{e}{\pi^2}\int_{\omega_{\text{g}}}^{\infty}\frac{d\omega}{2\pi}\left[\phi(\omega,T_{\text{R}})-\phi(\omega-\omega_0,T_{\text{N}})\right]\left[\int_{\omega/c}^{\infty}d\beta s_{\text{Evan}}+\int_0^{\omega/c}d\beta s_{\text{Prop}}\right]. \tag{13}$$

Based on Eq. (13), the power output P_{N} of the NFTC can be expressed as [22, 30, 31]

$$P_{\text{N}}=V_{\text{N}}J_{\text{N}}A_{\text{N}}. \tag{14}$$

2.3 The power output and efficiency of the coupled system

According to the first law of thermodynamics, an energy balance equation is determined as

$$-\Delta\dot{H} - P_{\mathrm{F}} - q_{\mathrm{L}} = q_{\mathrm{N}} = q_{\mathrm{Evan}} + q_{\mathrm{Prop}} , \tag{15}$$

where $q_{\mathrm{L}} = (A_{\mathrm{F}} - A_{\mathrm{N}})\left[U\left(T_{\mathrm{F}}^4 - T_{\mathrm{A}}^4\right)\right]$ is the heat leak. $U = 2.8\times10^{-9}\,\mathrm{Wcm^{-2}K^{-4}}$ is the effective heat transfer coefficient. Only when $-\Delta\dot{H} - P_{\mathrm{F}} - q_{\mathrm{L}} > 0$, the NFTC can be driven. Hence, an inequation can be derived as

$$-\Delta h J_{\mathrm{F}}/(NF) - V_{\mathrm{F}} J_{\mathrm{F}} - (1 - A_{\mathrm{N}}/A_{\mathrm{F}})\left[U\left(T_{\mathrm{F}}^4 - T_{\mathrm{A}}^4\right)\right] > 0 , \tag{16}$$

Through numerical analysis, one can find that there exists a start-up current density $J_{\mathrm{F,su}}$ of the SOFC. Only when $J_{\mathrm{F}} > J_{\mathrm{F,su}}$, the system can work at coupled state. On the other hand, Eq. (15) shows that three parameters V_{N}, V_{F}, and $A_{\mathrm{F}}/A_{\mathrm{N}}$ are coupled with each other when relevant parameters are given. Inserting Eqs. (2)-(12) into Eq. (16), $A_{\mathrm{F}}/A_{\mathrm{N}}$ can be determined for given two voltages V_{F} and V_{N}.

Using Eqs. (1), (2), and (14), one can derive the power output and efficiency of the coupled system as

$$P = P_{\mathrm{F}} + P_{\mathrm{N}} = \left(V_{\mathrm{Rev}} - V_{\mathrm{act}} - V_{\mathrm{con}} - V_{\mathrm{ohm}}\right) J_{\mathrm{F}} A_{\mathrm{F}} + V_{\mathrm{N}} J_{\mathrm{N}} A_{\mathrm{N}} \tag{17}$$

and

$$\eta = \frac{P}{-\Delta\dot{H}} = \frac{\left(V_{\mathrm{Rev}} - V_{\mathrm{act}} - V_{\mathrm{con}} - V_{\mathrm{ohm}}\right) J_{\mathrm{F}} A_{\mathrm{F}} + V_{\mathrm{N}} J_{\mathrm{N}} A_{\mathrm{N}}}{-\Delta h J_{\mathrm{F}} A_{\mathrm{F}}/(NF)} . \tag{18}$$

Equations (14)-(18) can be directly used to analyze the optimum performance of the coupled system.

3. Optimum performance analyses

Using Eqs. (15), (17), and (18), the dependences of area ratio $A_{\mathrm{F}}/A_{\mathrm{N}}$, the power output density P^*, and the efficiency η on V_{F} and V_{N} can be obtained, as shown in Fig. 2. In Fig. 2(a), $A_{\mathrm{F}}/A_{\mathrm{N}}$ decreases with increasing V_{N} at a given V_{F}, because the increase of V_{N} increases the electrochemical potential eV_{N} of the infrared photons and decreases the near-field radiative heat flow

q_N [32, 33]. Consequently, the coupled system should decrease A_F/A_N to meet the energy balance Eq. (15). Fig. 2(a) shows that A_F/A_N increases with increasing V_F at a given V_N, because the increase of V_N decreases the waste heat flow $\left(-\Delta\dot{H}-P_F\right)$, and thus, the coupled system should increase A_F/A_N to meet the energy balance Eq. (15). One can find from Fig. 2(b) that the voltages V_F and V_N of the two subsystems can be optimized to obtain a maximum power density P^*_{max}. Because the power output of the coupling system is mainly delivered by the SOFC, the effciency η_F is a monotonic increasing function of V_F, and thus, one can only optimize V_N to obtain a local maximum efficiency for a given V_F, while η increases monotonically with increasing V_F, as verified in Fig. 2(c).

In order to dedermine to optimal work regions, the curves of P^*, P^*_F, η_F, and η as a function of J_F are shown in Fig. 3, where the parameters A_F/A_N, V_F, V_N, and J_N have been optimized. In Fig. 3(a), $J_{F,P}$ and $(A_F/A_N)_P$ are the values of J_F and A_F/A_N at the maximum power output density P^*_{max}, $J_{F,ub}$ and $(A_F/A_N)_{lb}$ are the upper bound current density and the lower bound area ratio, $J_{F,lb}$ and $(A_F/A_N)_{ub}$ are the lower bound current density and the upper bound area ratio when the power output density P^* of the coupled system is equal to the maximum power output density $P^*_{F,max}$ of the SOFC. Fig. 3(a) shows that only when J_F is located in the region $J_{F,su} < J_F \le J_{F,ub}$, can the coupled system work normally. It is clearly observed from Fig. 3(a) that P^* is not a monotonic function of J_F and A_F/A_N, and consequently, there exists a maximum power output density $P^*_{max} = 1.01\,\mathrm{Wcm^{-2}}$. According to Eq. (15) and the values $(A_F/A_N)_P$=5.63 and $J_{F,P}$=1.95 $\mathrm{Acm^{-2}}$, the optimal value $V_{F,P} = 0.180\,\mathrm{V}$ and $V_{N,P} = 0.255\,\mathrm{V}$ can be obtained. In Fig. 3(b), η_{ub} is the upper efficiency when J_F=$J_{F,lb}$ and $P^* = P^*_{F,max}$; η_P is the efficiency when $P^* = P^*_{max}$. The calculated result $\left(P^* - P^*_{F,max}\right)/P^*_{F,max}$ =79.8% indicates that the power output density has been significantly improved. Fig. 3 shows that the efficiencies of the single SOFC operated in the region of $J_F < J_{F,su}$ are larger than the efficiencies of the coupled system operated in the region of $J_{\mathrm{F,su}} < J_{\mathrm{F}} \le J_{\mathrm{F,ub}}$. However, the power output density is very small in the region of $J_{\mathrm{F}} < J_{\mathrm{F,su}}$. Obviously, when $J_{\mathrm{F}} < J_{\mathrm{F,lb}}$ and $A_{\mathrm{F}}/A_{\mathrm{N}} > (A_{\mathrm{F}}/A_{\mathrm{N}})_{\mathrm{ub}}$, both the power output density P^* of the coupled system is smaller than $P^*_{\mathrm{F,max}}$ of the SOFC, and consequently, the coupled system operating in such a region is not significant. When $J_{\mathrm{F,P}} < J_{\mathrm{F}} < J_{\mathrm{F,ub}}$ and $(A_{\mathrm{F}}/A_{\mathrm{N}})_{\mathrm{P}} > A_{\mathrm{F}}/A_{\mathrm{N}} > (A_{\mathrm{F}}/A_{\mathrm{N}})_{\mathrm{lb}}$, $P^* > P^*_{\mathrm{F,max}}$, both the efficiency and the power output density of the coupled system decrease with the increasing J_{F}, and the coupled system cannot be allowed to operate in this region. Thus, the optimal regions of J_{F} and $A_{\mathrm{F}}/A_{\mathrm{N}}$ should be

$$J_{\mathrm{F,lb}} < J_{\mathrm{F}} \le J_{\mathrm{F,P}} \tag{19}$$

and

$$(A_{\mathrm{F}}/A_{\mathrm{N}})_{\mathrm{ub}} > A_{\mathrm{F}}/A_{\mathrm{N}} \ge (A_{\mathrm{F}}/A_{\mathrm{N}})_{\mathrm{P}} . \tag{20}$$

According to the inequations (19) and (20), the power output density and the efficiency of the coupled can be determined as

$$P^*_{\mathrm{max}} \ge P^* > P^*_{\mathrm{F,max}} \tag{21}$$

and

$$\eta_{\mathrm{ub}} > \eta \ge \eta_{\mathrm{P}} . \tag{22}$$

The effects of the vacuum gap d on the maximum power output density and the optimum operating conditions of the coupled system are shown in Fig. 4. It is seen from Fig. 4(a) that $(A_{\mathrm{F}}/A_{\mathrm{N}})_{\mathrm{P}}$ monotonically decreases with increase of d, because the enhancement of A_{N} based on the photon tunneling effect is not significant as the NFTC with a large d. Fig. 4(a) displays that P^*_{max} firstly decreases, and then increases as d transition from near-field to far-field, finally changes negligibly with increase of d. The maximum power density in the near-field is 1.3 times than that in the far-field. The result indicates that integrating NFTC with the SOFC to form the coupled system is significant for enhancing the overall system efficiency. The variations of $V_{\mathrm{F,P}}$ and $V_{\mathrm{N,P}}$ with d

depend on the relations $P^*_{\max} \sim d$ and $(A_F/A_N)_P \sim d$. Because the emitter radiates the photons flow and the heat flow towards the PV cell from the near-field to the far-field, thus, the curves of $(A_F/A_N)_P$, $V_{F,P}$ and $V_{N,P}$ varying with d are not smooth, as shown in Fig. 4(b).

When the vacuum gap is sufficiently larger than the characteristic wavelength of thermal radiation given by Wien's displacement law, i.e., the far-field limit condition, the simplified heat flow q_N and current density J_N are, respectively, expressed as [34, 35]

$$q_N = \frac{A_N}{4\pi^2\hbar^2c^3}\int_0^\infty \left[\frac{E^3}{\exp\left[E/(KT_R)\right]-1} - \frac{E^3}{\exp\left[(E-V_N e)/(KT_N)\right]-1}\right]dE \tag{23}$$

and

$$J_N = \frac{e}{4\pi^2\hbar^2c^3}\int_{E_g}^\infty \left[\frac{E^2}{\exp\left[E/(KT_R)\right]-1} - \frac{E^2}{\exp\left[(E-V_N e)/(KT_N)\right]-1}\right]dE\,, \tag{24}$$

By re-writing Eqs. (23) and (24), the maximum power density $P^*_{\max}=0.755\,\mathrm{Wcm^{-2}}$ and the corresponding conditions $(A_F/A_N)_P=5.29$, $V_{F,P}=0.295\,\mathrm{V}$, and $V_{N,P}=0.249\,\mathrm{V}$ can be calculated. Combining the calculated result and Fig. 4(a), one can find that $P^*_{\max}$, $(A_F/A_N)_P$, and $V_{N,P}$ of the near-field coupled system are larger than that of the far-field coupled system, whereas the optimum value $V_{F,P}$ of the near-field coupled system is smaller than the that of the far-field coupled system. As the photon tunneling effect in the far-field regime can be neglected, the radiative heat flow and the current density are not enhanced. The far-field coupled system needs a small value $(A_F/A_N)_P$ to meet the thermal balance equation, i.e., Eq. (15).

4. Discussion

Table 2 shows that $V_{F,P}$, $P^*_{\max}$, η_{ub}, and η_P are not a monotonic function of T_F when T_F varies in the range of 873~1273 K. Further, one can find that $(A_F/A_N)_P$ and $V_{N,P}$ increase as T_F is increased. An objective function $Z=P^*_{\max}\times\eta_{ub}$ is introduced to make a trade-off between the power density and the efficiency. One can discover that there exists a maximum value of Z and the corresponding optimum T_F. The result indicates that the temperature T_F is of great importance for the design of the coupling system. By using the regenerator, the SOFC temperature can be adjusted to approach the optimum temperature.

In order to expound that the performance of the coupled system mentioned here is better than that of other SOFC-based coupled systems, we calculate the maximum power densities P^*_{max} of the coupled system operated at several temperatures T_F (e.g., 873 K, 1073 K, 1173 K, and 1273 K), as shown in Fig. 5. The curve connected by these points in Fig. 5 can be used to indicate the maximum power output densities of the SOFC-NFTC coupled system operated in the normal operating temperature range of SOFC. For the convenience of comparison, the maximum power output densities P^*_{max} of other SOFC-based coupled systems operated at different temperatures T_F are marked on Fig. 5. In addition to SOFC-gas turbine and SOFC-Brayton coupled systems, the maximum power output densities of the coupled system mentioned here are larger than those of other SOFC-based coupled systems. More importantly, the SOFC-NFTC coupled system owns the advantages of small-size, simple design, low noise, easy maintenance, etc. and consequently, theoretical simulation on the SOFC-NFTC coupled system is very significant and the experimental investigation including the optimum matching of two subsystems can be easily carried out.

5. Conclusions

A new energy system consisting of an SOFC and a NFTC has been proposed and theoretically evaluated. The main results are listed as follows:

(1) According to the energy balance equation, the relations between the output voltages of the subsystems and the area ratio of the SOFC to the NFTC are revealed, and the start-up current density of the SOFC is numerically determined.

(2) The performance characteristics of the SOFC-NFTC coupled system are studied by numerically.

The maximum power output density $P^*_{\max} = 1.01\,\mathrm{Wcm^{-2}}$ and the corresponding optimum conditions $(A_F/A_N)_P = 5.63$, $J_{F,P} = 1.95\,\mathrm{Acm^{-2}}$, $V_{F,P} = 0.180\,\mathrm{V}$, and $V_{N,P} = 0.255\,\mathrm{V}$ are obtained. By comparing to the single SOFC, the power output density is increased by 79.3%, and the optimally working regions of key prameters are presented as Eqs. (19)-(21). The effects of the NFTC's vacuum gap on the optimum performance of the coupled system are discussed.

(3) The far-field performance limit of the coupled system is studied. The results reveal that the coupled system operated at near-field regime is better than it operated at far-field regime.

(4) The maximum power output densities of the SOFC-NFTC coupled system operated at different temperatures are compared with those of other SOFC-based coupled systems.

In summary, the results obtained in present work show that the SOFC-NFTC coupled systems have some advantages over other SOFC-based coupled systems and are worth to be further investigated.

Acknowledgements

This work has been supported by the Science and Technology Research Program of Chongqing Municipal Education Commission (Grant No. KJQN201901144) and the Scientific Research Foundation of Chongqing University of Technology (Grant No. 2019ZD22), People's Republic of China. M. Ni thanks the funding support from Hong Kong Polytechnic University (P0014036) and a grant (Project Number: PolyU 152064/18E) from Research Grant Council, University Grants Committee, Hong Kong SAR.

References

[1] P. Boldrin, N. P. Brandon, Nature Catalysis 2 (2019) 571.

[2] C. Bao, Z. Jiang, X. Zhang, J. Power Sources 294 (2015) 317–332.

[3] M. Ni, Int. J. Hydrogen Energy. 37(8)(2012) 6389-6399.

[4] M. Ni, J. Power Sources 202(2012) 209-216.

[5] K. Huang, S. C. Singhal, J. Power Sources 237 (2013) 84–97.

[6] Y. Zhao, J. Chen, J. Power Sources 186 (2009) 96–103.

[7] X. Chen, Y. Pan, J. Chen, Fuel Cell 10 (2010) 1164–1170.

[8] H. Zhang, H. Xu, B. Chen, F. Dong M. Ni, Energy 132 (2017) 280–288.

[9] Y. Wang, L. Cai, T. Liu, J. Wang, J. Chen, Energy 93 (2015) 900–907.

[10] X. Zhang, Y. Wang, T. Liu, J. Chen, Energy Convers. Manage. 86 (2014) 1102–1109.

[11] X. Chen, B. Lin, J. Chen, Energy Fuels 23 (2009) 6079–6084.

[12] E. Açıkkalp, Energy Convers. Manage. 148 (2017) 279–286.

[13] D. F. Waters, Christopher P. Cadou, J. Power Sources 221 (2013) 272–283.

[14] T. Liao, L. Cai, Y. Zhao, J. Chen, J. Power Sources 306 (2016) 666–673.

[15] R. Messina, P. Ben-Abdallah, Sci. Rep. 3 (2013) 1383.

[16] A. Datas, R. Vaillon, Nano Energy 61 (2019) 10–17.

[17] A. Datas, R. Vaillon, Appl. Phys. Lett. 114 (2019) 133501.

[18] T. Liao, X. Zhang, X. Chen, J. Chen. J. Appl. Phys. 125 (2019) 203103.

[19] M. P. Bernardi, D. Milovich, M. Francoeur, Nat. Commun. 7, (2016) 12900.

[20] B. Song, D. Thompson, A. Fiorino, Y. Ganjeh, P. Reddy, E. Meyhofer, Nat. Nanotechnol. 11, (2016) 509–514.

[21] A. Fiorino, D. Thompson, L. Zhu, B. Song, P. Reddy, E. Meyhofer, Nano Lett. 18, (2018) 3711.

[22] A. Fiorino, L. Zhu, D. Thompson, R. Mittapally, P. Reddy, E. Meyhofer, Nat. Nanotechnol. 13, (2018) 806–811.

[23] D. A. Noren, M. A. Hoffman, J. Power Sources 152 (2005) 175–181.

[24] F. Calise, A. Palombo, L. Vanoli, J. Power Sources 158 (2006) 225–244.

[25] C. Wang, M. H. Nehrir, S. R. Shaw, IEEE Trans. Energy Conv. 20 (2005) 442–451.

[26] Y. Ji, K. Yuan, J. N. Chung, Y. C. Chen, J. Power Sources 161 (2006) 380–391.

[27] H. Zhu, R. J. Kee, J. Power Sources 117 (2003) 61–74.

[28] S. J. Watowich, R. S. Berry, J. Phys. Chem. 90 (1986) 4624–4631.

[29] M. Ni, M. K. H. Leung, D. Y. C. Leung, Energy Convers. Manage. 48 (2007) 1525–1535.

[30] T. Liao, Z. Yang, Q. Dong, X. Chen, J. Chen, IEEE Transac. Electron Devices 64 (2017) 4144–4148.

[31] T. Liao, Z. Yang, W. Peng, X. Chen, J. Chen, Energy Convers. Manage. 152 (2017) 214–220.

[32] P. Würfel, J. Phys. C: Solid State Physics 15 (1982) 3967–3985.

[33] E. Tervo, E. Bagherisereshki, Z. Zhang, Front. Energy 12 (2018) 5-21

[34] X. Zhai, J. Lai, H. Liang, S. Chen, J .Appl. Phys. 108 (2010) 074507.

[35] P. F. Baldasaro, J. E. Raynolds, G. W. Charache, D. M. DePoy, C. T. Ballinger, T. Donovan, J. M. Borrego, J. Appl. Phys. 89 (2001) 3319.

List of Tables

List of Figures

Table 1. The operating conditions and parameters of the SOFC [6, 7, 25].

Parameter	Value
SOFC temperature, T_F (K)	1073
Fuel composition pressures, p_{H_2} (atm); p_{H_2O} (atm)	0.97; 0.03
Air composition pressures, p_{O_2} (atm); p_{N_2} (atm)	0.21; 0.79
Cathode exchange current density, $J_{e,a}$ (Acm^{-2})	0.53
Anode exchange current density, $J_{e,c}$ (Acm^{-2})	0.20
Electrolyte thickness, L_{et} (cm)	2×10^{-3}
Activation energy of O^{2-}, W_{ae} (J mol^{-1})	8.0×10^{4}
Ionic conductivity of O^{2-}, σ(S cm^{-1})	3.6×10^{5}
Cathode limiting current density, $J_{L,a}$ (A cm^{-2})	2.99
Anode limiting current density, $J_{L,c}$ (A cm^{-2})	2.16
Standard molar enthalpy change at 1073K, Δh(J mol^{-1})	-248303
Standard molar Gibbs free energy change at 1073k, Δg(J mol^{-1})	-188680

Table 2. The key parameters of the SOFC-NFTC coupling system with varying T_{F}, where $d = 100\,\mathrm{nm}$.

$T_{\mathrm{F}}\,(\mathrm{K})$	$V_{\mathrm{F,P}}\,(\mathrm{V})$	$V_{\mathrm{N,P}}\,(\mathrm{V})$	$(A_{\mathrm{F}}/A_{\mathrm{N}})_{\mathrm{P}}$	$P^{*}_{\max}\,(\mathrm{Wcm^{-2}})$	η_{ub}	η_{P}
873	0.158	0.225	2.59	0.647	0.542	0.340
1073	0.180	0.255	5.63	1.01	0.548	0.402
1173	0.252	0.266	9.55	1.13	0.532	0.439
1273	0.127	0.276	11.6	0.742	0.341	0.301

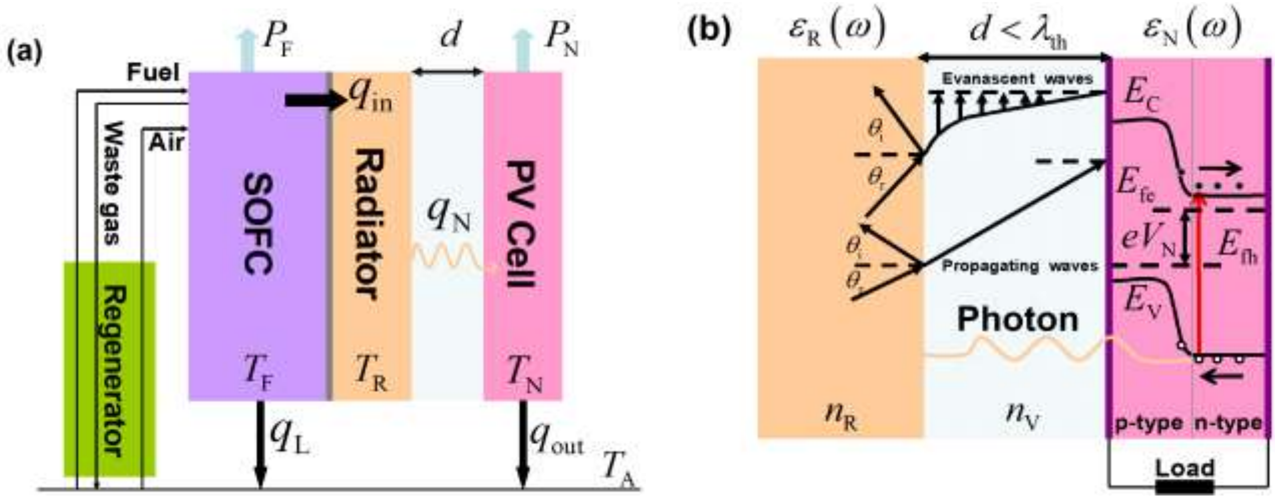

Fig. 1. (a)The schematic diagram of a SOFC-NFTC coupled system and (b) the working principle of NFTC.

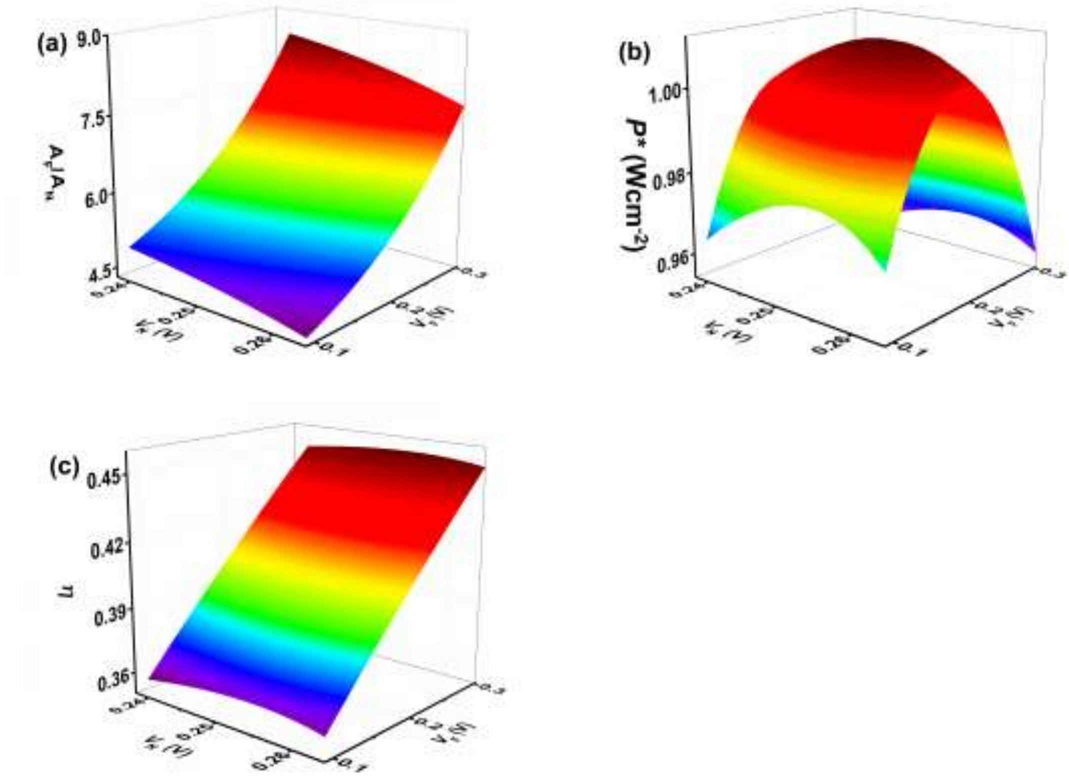

Fig. 2. Three-dimensional graphs of (a) the area ratio A_F/A_N, (b) the power output density $P^* = P/A_F$, (c) the efficiency η varying with V_F and V_N, where $\hbar\omega_g = E_g = 0.36\,\mathrm{eV}$ and $d = 100\,\mathrm{nm}$.

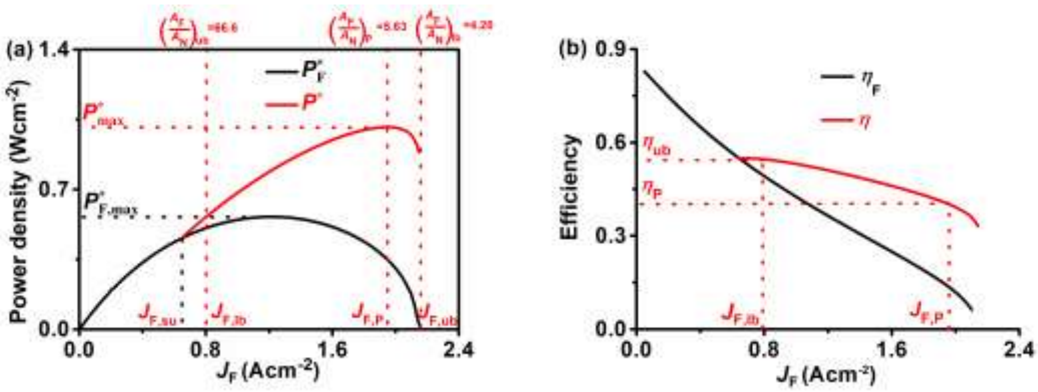

Fig. 3. The curves of (a) P^* and $P_F^* = P_F / A_F$ and (b) η and η_F varying with J_F.

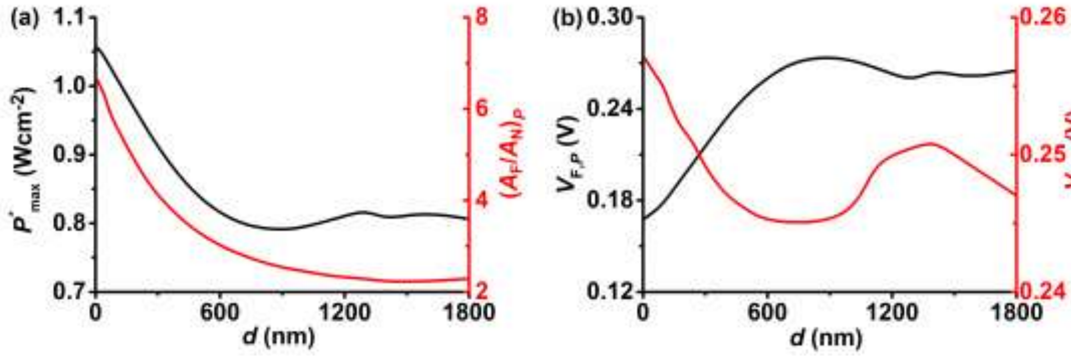

Fig. 4. The curves of (a) $P^*_{\max}$ and $(A_F/A_N)_P$ of the coupled system and (b) $V_{F,P}$ and $V_{N,P}$ varying with the vacuum gap d.

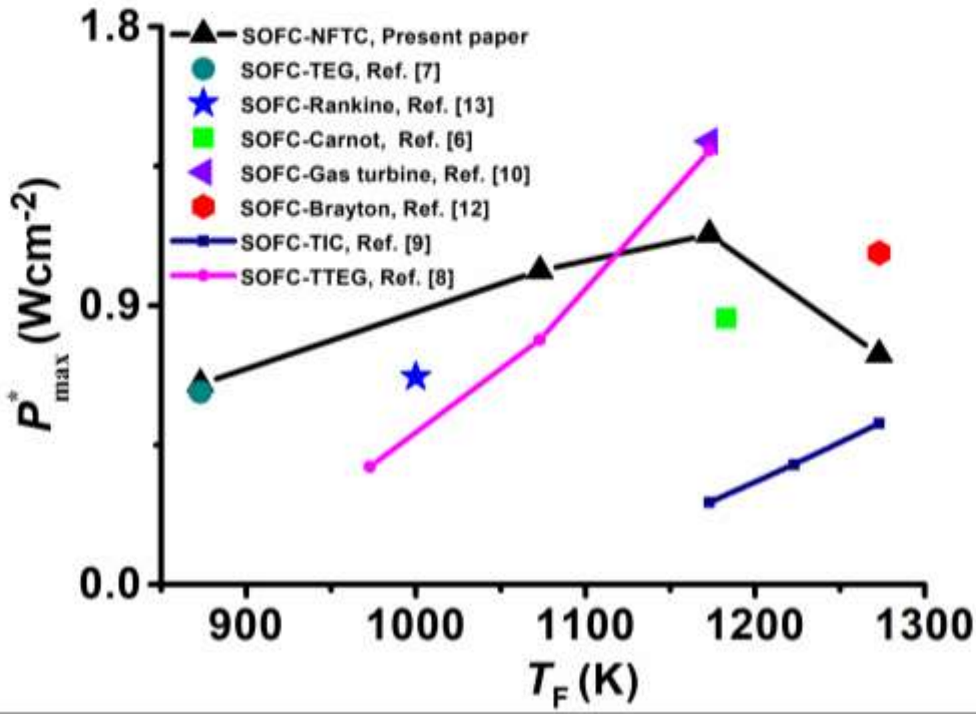

Fig. 5. The comparison of the maximum power output densities of various SOFC-based coupled systems.